

## Dark matter halos of luminous AGNs from galaxy-galaxy lensing with the HSC Subaru Strategic Program

WENTAO LUO,<sup>1,2</sup> JOHN D. SILVERMAN,<sup>3,4</sup> SURHUD MORE,<sup>5,3</sup> ANDY GOULDING,<sup>6</sup> HIRONAO MIYATAKE,<sup>3,7,8</sup>  
TAKAHIRO NISHIMICHI,<sup>9,3</sup> CHIAKI HIKAGE,<sup>3</sup> LALITWADEE KAWINWANICHAKIJ,<sup>3</sup> JUNYAO LI,<sup>3,2</sup> XIANGCHONG LI,<sup>3</sup>  
ELINOR MEDEZINSKI,<sup>6</sup> MASAMUNE OGURI,<sup>10,11,3</sup> TAIRA OOGI,<sup>3</sup> AND CRISTOBAL SIFON<sup>6</sup>

<sup>1</sup>*Kavli Institute for the Physics and Mathematics of the Universe, The University of Tokyo, Kashiwa, Japan 277-8583 (Kavli IPMU, WPI)*

<sup>2</sup>*Department of Astronomy, School of Physical Sciences, University of Science and Technology of China, Hefei, Anhui 230026, China*

<sup>3</sup>*Institute for the Physics and Mathematics of the Universe (Kavli IPMU, WPI), UTIAS, Tokyo Institutes for Advanced Study, University of Tokyo, Chiba, 277-8583, Japan*

<sup>4</sup>*Department of Astronomy, School of Science, The University of Tokyo, 7-3-1 Hongo, Bunkyo, Tokyo 113-0033, Japan*

<sup>5</sup>*IUCAA, Post Bag 4 Ganeshkhind, Savitribai Phule Pune University Campus Pune 411 007, India*

<sup>6</sup>*Department of Astrophysical Sciences, Peyton Hall Princeton University, 08544 NJ, USA*

<sup>7</sup>*Institute for Advanced Research, Nagoya University, Nagoya 464-8601, Japan*

<sup>8</sup>*Division of Physics and Astrophysical Science, Graduate School of Science, Nagoya University, Nagoya 464-8602, Japan*

<sup>9</sup>*Center for Gravitational Physics, Yukawa Institute for Theoretical Physics, Kyoto University, Kyoto 606-8502, Japan*

<sup>10</sup>*Research Center for the Early Universe, University of Tokyo, Tokyo 113-0033, Japan*

<sup>11</sup>*Department of Physics, University of Tokyo, Tokyo 113-0033, Japan*

### ABSTRACT

We assess the dark matter halo masses of luminous AGNs over the redshift range 0.2 to 1.2 using galaxy-galaxy lensing based on imaging data from the Hyper Suprime-Cam Subaru Stragic Program (HSC-SSP). We measure the weak lensing signal of a sample of 8882 AGNs constructed using HSC and WISE photometry. The lensing detection around AGNs has a signal to noise ratio of 15. As expected, we find that the lensing mass profile is consistent with that of massive galaxies ( $M_* \sim 10.8 M_\odot$ ). Surprisingly, the lensing signal remains unchanged when the AGN sample is split into low and high stellar mass hosts. Specifically, we find that the **excess surface density (ESD)** of AGNs, residing in galaxies with high stellar masses, significantly differs from that of the control sample. We further fit a halo occupation distribution model to the data to infer the posterior distribution of parameters including the average halo mass. We find that the characteristic halo mass of the full AGN population lies near the knee ( $\log(M_h/h^{-1}M_\odot) = 12.0$ ) of the stellar-to-halo mass relation (SHMR). Illustrative of the results given above, the halo masses of AGNs residing in host galaxies with high stellar masses (i.e., above the knee of the SHMR) falls below the calibrated SHMR while the halo mass of the low stellar mass sample is more consistent with the established SHMR. These results indicate that massive halos with higher clustering bias tends to suppress AGN activity, probably due to the lack of available gas.

*Keywords:* (cosmology:) dark matter; gravitational lensing: weak; galaxies: active

### 1. INTRODUCTION

Supermassive black holes (SMBHs) power the most energetic phenomena in our universe, i.e. active galactic nuclei (AGNs) and luminous quasars. Their formation and growth is intimately related to the galaxies in

which they reside. This is seen in the observed relations of the masses of SMBHs to the properties (stellar mass, bulge mass, velocity dispersion) of their host galaxies (see [Kormendy & Ho 2013](#), for a review on this topic). Simply, the more massive black holes sit in the centers of galaxies with high stellar masses. Closely related, there is a preference for AGNs to be associated with massive galaxies that are still forming new stars (e.g.,

Silverman et al. 2009a; Mullaney et al. 2012; Xie et al. 2021); this may indicate a scenario where concurrent fueling of SMBHs and star formation is occurring through shared gas reservoirs (galactic scale or larger; Schulze et al. 2019; Carraro et al. 2020; Shangguan et al. 2020 and/or galaxy mergers (e.g., Hopkins et al. 2008; Goulding et al. 2018). Subsequently, the effective shutdown in mass growth of the SMBH and its host is attributed to some form of feedback from the SMBH itself (e.g., King & Pounds 2015; Ishibashi et al. 2021). With much attention on the low redshift universe, many efforts have begun to establish these relations out to the peak of the cosmic star formation history and beyond to the epoch of reionization.

There is also much interest to determine whether the growth of SMBHs may be influenced by their larger-scale environment (e.g., Kauffmann et al. 2004; Khabiboulline et al. 2014). In particular, clustering measurements of quasars have provided insight on their dark matter halos using samples selected from wide-area spectroscopic surveys such as 2dF (Folkes et al. 1999), SDSS (York et al. 2000), BOSS (Pâris et al. 2012) and eBOSS (Myers et al. 2015). Optically-selected quasars samples have a preference for halo masses of a few times  $10^{12} M_{\odot}$ , and an evolving bias consistent with this halo mass scale at most redshifts (Shen et al. 2007, 2009; Ross et al. 2009; Eftekharzadeh et al. 2015; Rodríguez-Torres et al. 2017). Remarkably, this halo mass scale coincides with the peak in the SHMR (Behroozi et al. 2012; Behroozi et al. 2019), indicating a mass scale where halos are most efficient at converting gas into stars.

It is also necessary to understand the connection between AGN and dark matter halos with consideration of the stellar mass of the AGN host galaxies (e.g., Allevato et al. 2019; Aird & Coil 2021a) which can be obtained through SED model fitting (Goulding et al. 2018) or two-dimensional image decomposition (e.g., Li et al. 2021a). Recently, Krishnan et al. (2020) show that the host galaxies of quasars dictate the clustering of X-ray AGNs hence their dark matter property. They study the inferred bias for AGNs and claim that AGNs lie between matched star-forming and passive galaxy populations since their hosts are simply a mixture of the two populations.

As well, there has been much interest to probe the environmental differences between various AGN populations (e.g., obscured and unobscured). For example, the clustering measurements of X-ray AGNs out to  $z \sim 2$  show that the obscured AGNs have similar clustering properties as their unobscured counterparts (Hickox et al. 2011; Koutoulidis et al. 2018). These claims appear to be robust given further effort by DiPompeo

et al. (2017a) using a half million WISE-selected AGNs centered at  $z=1$ . Mendez et al. (2016) expanded such studies to X-ray, IR and radio selected AGNs and also found no significant difference between obscured and unobscured AGNs while matching on stellar mass and star formation rate (SFR). Alternatively, Allevato et al. (2019) find a negative dependence of the large-scale bias on SFR using obscured AGN which may be expected since gas levels in galaxies will be suppressed in denser environments. Interestingly, Jiang et al. (2016) detect stronger clustering for obscured AGNs at scales smaller than  $100 \text{ kpc}/h$  and Krumpe et al. (2018) detect stronger clustering for high X-ray luminosity AGNs also at smaller scales. Furthermore, Powell et al. (2018) claim a difference in clustering between the obscured and unobscured AGNs at the same luminosity, redshift, stellar mass and Eddington ratio. They also study the relation between the black hole mass and galaxy properties and conclude that massive black holes tend to reside in central galaxies. In addition, Shirasaki et al. (2018) find no obvious dependence of clustering on black hole mass.

To extract further information from clustering measurements, proper modeling (i.e., halo occupation distributions - HOD; Zheng et al. 2007; Zu & Mandelbaum 2015; DiPompeo et al. 2017b; Alam et al. 2020) allows one to understand not only the halo mass, but the contribution of the 1-halo term (within the virial radius), 2-halo term (scale beyond the virial radius) and the satellite fraction. In recent HOD modeling efforts (e.g., Zu & Mandelbaum 2015; Alam et al. 2020), various galaxy tracers have been used from the eBOSS survey (Ahumada et al. 2020). They find that quasars have larger satellite fraction than the other two tracers (LRGs, ELGs) and no environmental preference, whereas LRGs prefer denser environment and ELGs prefer less dense environment.

Complementary to clustering measurements, galaxy-galaxy lensing is a powerful tool for the direct detection of the underlying dark components of galaxies. The Sloan Digital Sky Survey (SDSS) (York et al. 2000) pioneered these studies (Sheldon et al. 2004; Mandelbaum et al. 2008; Luo et al. 2017, 2018) with the help of its wide area covering up to  $7500 \text{ deg}^2$ . Mandelbaum et al. (2009) measured the halo mass of optically- and radio-selected AGNs with the latter based on NVSS (Condon et al. 1998) and FIRST (Becker et al. 1995). They found that the halo mass of radio-loud AGNs is more than one magnitude larger than their optical counterparts and twice larger than a control sample with an identical stellar mass distribution. Since the SDSS imaging is too shallow to measure the galaxy-galaxy lensing

signal for high redshift objects, deep fields such as COSMOS (Scoville et al. 2007) provides imaging sufficient for weak lensing studies such as that of distant AGNs. For example, Leauthaud et al. (2015) measured the galaxy-galaxy lensing signal around moderate-luminosity X-ray-selected AGNs with  $z < 1.0$  from XMM-COSMOS (Cappelluti et al. 2009) and C-COSMOS (Elvis et al. 2009). A halo mass of  $10^{12.5} h^{-1} M_{\odot}$  for X-ray AGN is estimated by fitting a global Stellar-to-Halo mass Function (SHMF) (Leauthaud et al. 2012). However, the statistical significance is limited since the COSMOS field is only  $2 \text{ deg}^2$  thus the AGN sample size is relatively small (385) compared to the SDSS studies.

To overcome issues with sample size, the Hyper Suprime-Cam Subaru Strategic Program (HSC-SSP; Aihara et al. 2018) is designed particularly for weak lensing studies with a unique combination of wide area coverage, deep depths and superb seeing conditions. The  $i$ -band median seeing is  $0.58''$  and  $5\sigma$  detection down to  $i$ -band magnitude of 26, with weighted source number density of  $21.8 \text{ galaxies arcmin}^{-2}$ . The full-color full-depth area of the first public shape catalog-S16A (Mandelbaum et al. 2018a) covers  $136.9 \text{ deg}^2$  split in 6 separate regions overlapping with other surveys, i.e., XMM-Newton (Hasinger et al. 2001), HECTOMAP (Sohn et al. 2018b,a), GAMA09H, GAMA15H (Robotham et al. 2010), WIDE12H and VVDS (Le Fèvre et al. 2005), which was deliberately designed to maximize the weak lensing studies with ancillary information.

Here, we measure the galaxy-galaxy lensing signal of 8882 AGNs ranging in redshift from 0.2 to 1.2 as identified from HSC and WISE photometry using the S16a SSP data. We take advantage of the wide and deep imaging to study the lensing signal around AGNs further split into bins of stellar mass to investigate the stellar mass to halo mass relation of luminous AGNs. Equally important, we construct a control sample of 6,539,241 galaxies in HSC-SSP S16A fields by matching the 2D distribution in stellar mass and redshift. We then model the galaxy-galaxy lensing signals to extract information on the halo mass.

The structure of this paper is organized as follows. In Sec. 2, we present the data including the shape catalog from HSC-SSP S16A and the AGN hosts as foreground lenses. We also describe several basic properties of the foreground samples for AGNs and control galaxies. We specify the galaxy-galaxy lensing estimator in Sec. 3 and our forward modeling method in Sec. 4. The major results are presented in Sec. 5. We discuss these results in Sec. 6 and summarize the work in Sec. 7. Unless stated elsewhere, we adhere to using

PLANCK18 (Planck Collaboration et al. 2018) cosmology with  $\Omega_m = 0.315$ ,  $h = 0.674$ , and  $\sigma_8 = 0.810$ .

## 2. DATA

### 2.1. SUBARU HSC-SSP

The Hyper Suprime-Cam Subaru Strategic Program (HSC-SSP; Aihara et al. 2018, 2019) is an optical imaging survey of over 1000 square degrees in five optical bands (*grizy*) with the Subaru Telescope. The survey has three layers (Wide, Deep and UltraDeep) with depths reaching an AB magnitude of  $i \sim 26.4$ ,  $\sim 26.5$  and  $\sim 27.0 \text{ mag}$  ( $5\sigma$  for point source) respectively. The Wide survey regions target areas overlapping with other surveys, i.e. VVDS, XMM, GAMA09H, GAMA15H, HECTOMAP and WIDE12H.

The imaging data used in this paper is processed using the HSC pipeline (hscPipe 4.0.2; Bosch et al. 2018), which is based on the software built for LSST (Juric & Tyson 2015). The software removes instrumental effects such as flat-fielding, bias subtraction, the non-uniformity of plate scale, cosmic rays, and bad pixels. The major systematic in weak lensing measurement is inaccuracies in the determination of the Point Spread Function (PSF). The modeling of the PSF at the position of source galaxies is reconstructed using the PSFEx package developed by Bertin (2011). 20% of the stars are not used in the reconstruction but reserved to test the performance of the PSF reconstruction. The reconstruction of PSF is first performed on each exposure and then coadded in a consistent manner for the coadded images.

After the PSF is reconstructed, the source galaxy shapes are then measured using the re-Gaussianization technique Mandelbaum et al. (2018a) in order to generate the shape catalog of galaxies for weak lensing science. In order to evaluate the multiplicative bias ( $m$ ) and the additive bias ( $c$ ) of the shape measurement  $\gamma^{\text{obs}} = (1 + m)\gamma^{\text{true}} + c$ , a set of image simulations matching the properties of the HSC survey are generated (Mandelbaum et al. 2018b) by using GalSim software (Rowe et al. 2015).

The final galaxy shape catalog has more than 12 million galaxies after several quality control cuts and covers a total area of  $136.9 \text{ square degree}$ . The posterior distribution for the photo- $z$  for each galaxy is estimated using six different methods as described in Tanaka et al. (2018), i.e. Direct Empirical Photometric code (DEmP Hsieh & Yee (2014)), Extended Photomet-

ric Redshift (Ephor<sup>1</sup>), Flexible Regression over Associated Neighbors with Kernel density estimation for Redshifts (FRANKEN-Z<sup>2</sup>), MLZ based on a self-organizing map (SOM Carrasco Kind & Brunner (2014)), Nearest Neighbors P(z) (NNPZ Cunha et al. (2009)) and Mizuki (Tanaka 2015). In this paper, we use the Mizuki photometric redshifts, which also provide a stellar mass estimate for each galaxy.

## 2.2. AGN sample

Luminous AGN are selected based on their optical photometry available in the HSC-SSP S18A catalog and matched to WISE photometry as described in Goulding et al. (2018). WISE provides imaging in the 3.4, 4.6, 12 and 22 $\mu$ m bands (Wright et al. 2010). For the AGN sample, WISE detections are required in the [3.4] and [4.6] bands with a signal-to-noise (S/N) greater than or similar to 4. The S/N is relaxed to 2.5 in the [12] band. Color-color selection is effective at identifying AGNs as shown in Figure 4 of Goulding et al. (2018). This is based on the two-color IR-AGN wedge defined by Mateos et al. (2012) that selects objects having a power-law continuum shape, characteristic of radiative-efficient AGNs. The selection is supplemented by AGN satisfying the single color cut by Stern et al. (2012). This selection enables the inclusion of both unobscured and obscured populations (see below) that effectively ensures that a sample size required to obtain a significant stacked weak-lensing signal, even when considering two separate bins (i.e., redshift, AGN luminosity, AGN type and host galaxy stellar mass) can be achieved. At this stage, there are 31532 AGNs identified over the HSC survey area in consideration.

We further restrict the sample to 30867 AGNs which also have measurements of the stellar mass of the host galaxy. The requirements of the HSC S16A full-depth, full-color region for weak lensing measurements reduce this number further to 15172 with  $\log L_{AGN}$  between 42.03 and 48.03 (based on fitting a power-law to the AGN mid-IR continuum). This allows us to address science goals such as the dependence of the halo mass on host stellar mass for AGNs as done in Leauthaud et al. (2015). We further limit the sample to those with redshifts between 0.2 and 1.2 to have sufficient background lensed galaxies to measure the stacked lensing signal of the foreground AGN sample. This results in a final sample of 8882 AGNs. Most of the reduction of the sample

**Table 1.** Basic properties of AGN samples.

Sample	Number	$\langle z \rangle$	$\langle \log(M_*) \rangle$
AGN all	8882	0.77	10.64
AGN I	3595	0.78	10.75
AGN II	3908	0.80	10.56
AGN $z \leq 0.60$	2554	0.44	10.57
AGN $z > 0.60$	6338	0.90	10.66
AGN $M_* \geq 10.65$	4618	0.81	10.96
AGN $M_* < 10.65$	4264	0.74	10.28
AGN $M_* \in (9.5, 10.5)$	3035	0.72	10.20
AGN $M_* \in (11.0, 12.0)$	1821	0.85	11.21
AGN $L_{AGN} \geq 44.7$	4445	0.97	10.72
AGN $L_{AGN} < 44.7$	4437	0.57	10.55
Gal.[8.9,9.3]	282636	0.52	9.18
Gal.[9.3,9.8]	441421	0.67	9.64
Gal.[9.8,10.3]	472763	0.63	10.12
Gal.[10.3,10.8]	352449	0.64	10.55
Gal.[10.8,11.3]	154808	0.66	10.97
Gal.[11.3,11.7]	27667	0.73	11.39

size is due to the smaller region of S16A compared to S18A.

Stellar mass estimates are carried out based on SED fitting using FAST with spectral templates. Goulding et al. (2018) found no significant bias between the stellar mass estimation of AGNs and non-AGN galaxies. In addition, we use the 2D image decompositions of their HSC images, available in Li et al. (2021a), for a subset of our sample to check whether the stellar masses of the hosts are in agreement between both methods. When dividing the AGN sample by host stellar mass, we generate a second set of high/low stellar mass bins with a wider separation in order to minimize the effect of the scatter on stellar mass estimation. The mean stellar masses of these two samples are 1.0 dex away from each other (Table 1).

## 2.3. Control sample of galaxies

The control sample of galaxies contains all objects from HSC-SSP DR1 with redshifts ranging from 0.2 to 1.2, similar to the AGN sample. The photometric redshift estimation of HSC-SSP DR1 (Tanaka et al. 2018) is based on Mizuki (Tanaka 2015), a SED-fitting code which uses a set of templates generated using stellar population synthesis models (Bruzual & Charlot 2003) under the assumption of a Chabrier IMF (Chabrier 2003) and the Calzetti dust attenuation (Calzetti et al. 2000) curve. Emission lines are added to the templates assuming solar metallicity (Inoue 2011). In addition to galaxy templates, they also include AGN templates generated by combining type I AGN spectrum from Polletta

<sup>1</sup> <https://hsc-release.mtk.nao.ac.jp/doc/index.php/photometric-redshifts/>

<sup>2</sup> <https://github.com/joshspeagle/frankenZ>

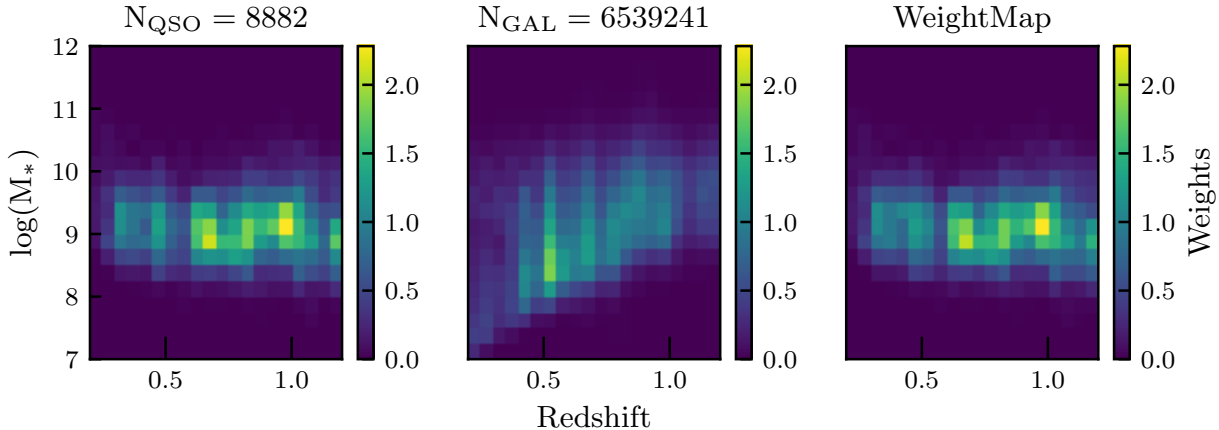


**Figure 1.** 2D density plot stellar mass and redshift with the corresponding weight map (*Left*: AGN, *Middle*: control galaxy sample, *Right*: weight map). Each panel has 21 by 21 bins with a minimum weight value of 0.003 and a maximum value of 2.28.

et al. (2007) and young galaxy templates from Bruzual & Charlot (2003).

We calculate the weak lensing signal using these photometric redshifts for the lens galaxies. Given that the control sample of galaxies does not have the same distribution in stellar mass and redshift (see left and middle panels of Fig. 1), we reweight the control sample of galaxies in order to match the 2D ( $21 \times 21$  bins) distribution of  $M_{stellar}$  ( $8.0 < \log M_{star} < 12.5$ ) and redshift ( $0.2 < z < 1.2$ ) of the AGN sample. The weight is the ratio between the number of the AGN and galaxies in each bin with smallest value of 0.003 and maximum weight value 2.28. This can be easily calculated such that

$$w_l = \frac{N_{qso}(z, M_{stellar})}{N_{gal}(z, M_{stellar})}. \quad (1)$$

In total, there are 6,539, 241 galaxies in this sample, so the signal-to-noise for the control sample is significantly higher than that of AGN sample. We have 9 bins in stellar mass, but discard the most massive with 2921 galaxies and the two least massive bins due to the small sample size (only 17570 and 89539 galaxies from the first stellar mass bin of the controlled galaxy samples with valid measurement of stellar mass) and therefore noisy measurements.

### 3. EXCESS SURFACE DENSITY(ESD) ESTIMATOR AND BACKGROUND SOURCE SELECTION

We describe the procedure to measure the galaxy-galaxy lensing signal using faint galaxies imaged by HSC including corrections for known systematics.

#### 3.1. Background sources

The shape catalog (Mandelbaum et al. 2018a) is based on  $i$ -band coadded images with the re-Gaussianization method (Hirata & Seljak 2003). The requirement of full-depth and full-color (FDFC) imaging results in an area coverage of  $136.9 \text{ deg}^2$ , which ensures a uniformity of the galaxy number density. As in Mandelbaum et al. (2018a), we limit the  $cmodel$  magnitude (see the definition in Bosch et al. (2018)) to  $i_{cmodel} < 24.5$ .

The measurement biases for each galaxy are calibrated based on the simulations generated by the software GalSim (Rowe et al. 2015). These biases include multiplicative bias  $m$ , additive bias ( $c_1, c_2$ ), shape measurement error  $\sigma_e$  and shape noise  $e_{rms}$  as a function of signal-to-noise ratio and resolution. In the simulations, realistic images from HST/ACS F814W images of the COSMOS field Leauthaud et al. (2007) are used to generate galaxies with various morphologies. The overall systematic uncertainty is around 1% (Mandelbaum et al. 2018b). As mentioned in Sec. 2.1, we choose Mizuki photometric redshift catalog, which is the only one contains stellar mass information among the six photometric catalogs.

#### 3.2. Estimator

The galaxy-galaxy lensing signal measures the differential profile of the projected mass density (i.e., Excess Surface Density; ESD)

$$\Delta\Sigma(R) = \bar{\Sigma}(\leq R) - \Sigma(R), \quad (2)$$

where  $\bar{\Sigma}(\leq R)$  is the average surface density averaged inside radius  $R$  and  $\Sigma(R)$  is the surface density at radius  $R$ . The signal around each galaxy sample can be measured by stacking the background shapes of galaxies

(Miyatake et al. 2019),

$$\Delta\Sigma(R) = \frac{1}{2\mathcal{R}(R)} \frac{\sum_l^{N_l} w_l \sum_s^{N_s} w_{ls} e_{t,ls} [\langle \Sigma_{cr}^{-1} \rangle_{ls}]^{-1}}{[1 + K(R)] \sum_l^{N_l} w_l \sum_s^{N_s} w_{ls}}, \quad (3)$$

where

- $e_{t,ls}$  is the tangential component of a source galaxy that is within projected distance  $R$  away from a lens galaxy.
- $\mathcal{R}(R) = 1 - \frac{\sum_l^{N_l} w_l \sum_s^{N_s} e_{rms}^2 w_{ls}}{\sum_l^{N_l} w_l \sum_s^{N_s} w_{ls}}$  is the responsivity of shape estimator which is  $\approx 0.84$ .
- $w_{ls}$  is the weight for each source galaxy,  $w_{ls} = (\langle \Sigma_{cr}^{-1} \rangle_{ls})^2 \frac{1}{\sigma_e^2 + e_{rms}^2}$ , as a function of  $\sigma_e$ ,  $e_{rms}$  and a geometric factor  $(\langle \Sigma_{cr}^{-1} \rangle_{ls})^2$ . ( $\sigma_e$ ,  $e_{rms}$  are the shape noise and shape measurement error.  $N_l$  and  $N_s$  are the stacked number of lens galaxies and source galaxies respectively.)
- $w_l$  is a weight for the lens sample. For quasars we chose a weight equal to unity, while for the control sample of galaxies, the weight is given by Equation 1.
- $\langle \Sigma_{cr}^{-1} \rangle_{ls}$  is calculated for each lens-source pair by applying the  $P(z)$  of the source to marginalize over photometric redshift errors,

$$\langle \Sigma_{cr}^{-1} \rangle_{ls} = \frac{\int_{z_l}^{\infty} \Sigma_{cr}^{-1}(z_l, z) P(z) dz}{\int_0^{\infty} P(z) dz} \quad (4)$$

- The factor  $K(R)$  accounts for the multiplicative bias calibrated from simulation

$$K(R) = \frac{\sum_l^{N_l} w_l \sum_s^{N_s} m_s w_{ls}}{\sum_l^{N_l} w_l \sum_s^{N_s} w_{ls}}. \quad (5)$$

Finally, we only select sources behind each lens that satisfy the requirement in Medezinski et al. (2018) where the accumulated probability of the photometric redshift  $P(z \geq z_l + 0.2)$  of each source is larger than 0.98,

$$P(z \geq z_l + 0.2) = \int_{z_l+0.2}^{\infty} p(z) dz \geq 0.98. \quad (6)$$

When measuring the lensing signals, we divide the projected radius into 10 equal logarithmic bins from 0.02Mpc/h to 2 Mpc/h.

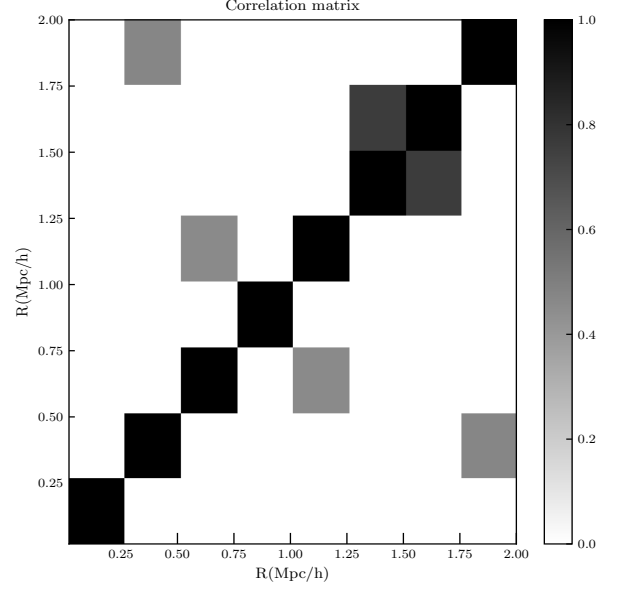


**Figure 2.** The covariance matrix calculated using 2000 bootstrap of 43 regions from S16A area divided by healpix.

### 3.2.1. Covariance matrix

We compute the covariance matrix from a bootstrap sample by dividing the sky using healpix<sup>3</sup> (Górski et al. 2005) into 43 subregions which balances the number of subsamples and the size that our measurement can reach (2Mpc/h) and then carry out a bootstrap routine (2000 times) to determine the covariance matrix. At small scale within virial radius of halos, the dominant error is the shape noise, at larger scale it has correlations caused by the large scale structure. The bootstrap sampling can capture all those features in correlation matrix. However, due to the smaller sample size, the covariance matrix is pretty noisy. We follow the treatment in Leauthaud et al. (2017) that truncates the correlation matrix with 0.2 as the threshold as in . Fig. 2. elucidates the correlation matrix that we use to build the likelihood function during the modeling process.

### 3.2.2. Photometric redshift bias correction

We use Miyatake et al. (2019) method to estimate the bias from photometric redshift errors, which is redshift dependent,

$$1 + b(z_l) = \frac{\Delta\Sigma}{\Delta\Sigma^{true}}(z_l) = \frac{\sum_{ls} w_{ls}^* \langle \Sigma_{cr,ls}^{-1} \rangle^{-1} [\Sigma_{cr,zl}^{true}]^{-1}}{\sum_{ls} w_{ls}^*} \quad (7)$$

The superscript *true* represents the "true" value of the geometry factor using the COSMOS region overlapping

<sup>3</sup> <https://healpix.sourceforge.io/>

with HSC-SSP S16A, and the weight  $w_{l_s}^*$  is provided in the PDR2 release based on a self-organizing map technique. We follow Miyatake et al. (2019) to use the  $w_{\text{SOM}} * w_{l_s}$  to calculate the bias in equation 7, such that

$$w_{l_s}^* = D_l^{-2} (1 + z_l)^{-2} \sum_s w_{\text{som}} w_{l_s}. \quad (8)$$

where the  $w_{\text{SOM}}$  is the weight generated based on self-organizing map (SOM, S. More et al 2022 in preparation) and  $w_{l_s}$  is the weight before multiplying by  $w_{\text{SOM}}$ . The final photometric redshift bias for each sample is then averaged over the redshift distribution as in equation 22 of Nakajima et al. (2012), where

$$\langle b_{\text{photoz}} \rangle = \frac{\int dz p(z_l) w_{l_s}^* b(z_l)}{\int dz p(z_l) w_{l_s}^*}. \quad (9)$$

Even though our sample is at relatively high redshift the photo-Z bias is low roughly about 2% which is consistent with Miyatake et al. (2019) and much smaller than the statistical error. And a correction of  $(1 + b_{\text{photoz}})$  is applied to the ESDs to correct for this bias.

#### 4. MODELS

In this section, we present the modeling scheme of the galaxy-galaxy lensing signals. In general we adopt the model following Mandelbaum et al. (2009) to extract the information of host halo mass, halo concentration, sub halo fraction. We fix the amplitude of the satellite HOD function because only the shape of the function matters after normalization in equation 17. We decompose the ESD into four components, the contribution of stellar mass at small scales, the subhalo and the host halo contribution, and the two halo term.

$$\Delta\Sigma(R) = \Delta\Sigma_{\text{stellar}}(R) + (1 - f_{\text{sat}})\Delta\Sigma_{\text{cen}}(R) + f_{\text{sat}}\Delta\Sigma_{\text{sat}}(R) + \Delta\Sigma_{2\text{halo}}(R) \quad (10)$$

We take the mean stellar mass of the lens samples as a point mass contributing to the ESD (Luo et al. 2018), due to the fact that the size of the galaxy is smaller than the scales relevant to our measurements, such that

$$\Delta\Sigma_{\text{stellar}}(R) = \frac{\langle M_{\text{stellar}} \rangle}{\pi R^2}. \quad (11)$$

$\Delta\Sigma_{\text{cen}}$  is the contribution of the halo given that the AGN or galaxy is located at the center of the halo. We use Yang et al. (2006) formulation to model the ESD, which assumes an NFW density profile

$$\rho(r) = \frac{\rho_0}{(r/r_s)(1 + r/r_s)^2}, \quad (12)$$

with  $\rho_0 = \frac{\bar{\rho}\Delta_{\text{vir}}}{3I}$ , where  $\Delta_{\text{vir}} = 200$ ,  $I = \frac{1}{c^3} \int_0^c \frac{x dx}{(1+x)^2}$ . Here  $c$  is the concentration parameter defined as the

ratio between the virial radius of a halo and its characteristic scale radius  $r_s$ . The projected surface density then can be analytically expressed (Yang et al. 2006) as :

$$\Delta\Sigma_{\text{cen}}(R) = \frac{M_h}{2\pi r_s^2 I} [g(x) - f(x)], \quad (13)$$

$$f(x) = \begin{cases} \frac{1}{x^2-1} \left[ 1 - \frac{\ln \frac{1+\sqrt{1-x^2}}{x}}{\sqrt{1-x^2}} \right] & x < 1 \\ \frac{1}{3} & x = 1 \\ \frac{1}{x^2-1} \left[ 1 - \frac{\tan^{-1}(\sqrt{x^2-1})}{\sqrt{x^2-1}} \right] & x > 1. \end{cases} \quad (14)$$

and

$$g(x) = \begin{cases} \frac{1}{x^2} \left[ \ln(x/2) + \frac{\ln \frac{1+\sqrt{1-x^2}}{x}}{\sqrt{1-x^2}} \right] & x < 1 \\ 2 + 2 \ln(\frac{1}{2}) & x = 1 \\ \frac{1}{x^2} \left[ \ln(x/2) + \frac{\tan^{-1}(\sqrt{x^2-1})}{\sqrt{x^2-1}} \right] & x > 1. \end{cases} \quad (15)$$

where  $x$  is the projected radius in units of  $r_s$ .

We model the satellite contribution as an off-centered host halo, for a fraction,  $f_{\text{sat}}$  of our samples. This effect can be simply treated as follows. The projected surface density will change from an NFW profile  $\Sigma_{\text{NFW}}(R)$  to

$$\Sigma_{\text{off}}(R|R_{\text{off}}) = \frac{1}{2\pi} \int_0^{2\pi} \Sigma_{\text{NFW}}(\sqrt{R^2 + R_{\text{off}}^2 + 2R_{\text{off}}R\cos\theta}) d\theta. \quad (16)$$

Here, we assume that the satellite galaxies are distributed in the same manner as the dark matter distribution, i.e., an NFW profile (see also Leauthaud et al. 2015). The resulting projected density profile is then the convolution between  $P(R_{\text{off}}|M_h)$  and  $\Sigma_{\text{host}}(R|R_{\text{off}})$ ,

$$\Sigma_{\text{sat}}(R) = \int_0^\infty n(M_h) \langle N_{\text{sat}} \rangle(M_h) dM_h \times \int dR_{\text{off}} P(R_{\text{off}}|M_h) \Sigma_{\text{off}}(R|R_{\text{off}}, M_h) \quad (17)$$

where  $P(R_{\text{off}}|M_h)$  can analytically be expressed with the help of  $f(x)$  in equation 14. The quantity  $\langle N_{\text{sat}} \rangle(M_h)$  is the occupation function of satellite galaxies given a halo mass  $M_h$  and  $n(M_h)$  is the halo mass function based on Tinker et al. (2005). We model the satellite HOD function following Eq. 12 in Mandelbaum et al. (2005), where

$$\langle N_{\text{sat}} \rangle(M_h) = \Theta^H(M_h - M_{\text{min}}) \left( \frac{M_h - M_{\text{min}}}{M'} \right)^\alpha \quad (18)$$

where  $\Theta^H(M_h - M_{\text{min}})$  is the Heaviside step function to set up the threshold with  $M_{\text{min}} = 3M_{\text{cen}}$  ( $M_{\text{cen}}$  denotes the central halo mass) which we set to be 3 time of the halo mass of the one for the  $\Delta\Sigma(R)_{\text{cen}}$  as in Mandelbaum et al. (2005) which is used to be the threshold of

major/minor merging systems. We also fix  $\alpha = 1$  following Mandelbaum et al. (2005). The difference between Mandelbaum et al. (2005) and our modeling is that we set the satellite fraction as a free parameter, while they fix it to be 0.2 as well as fixing  $M'$  to be a constant. So in total, there are three parameters in our model: the central halo mass, halo concentration, and the satellite fraction. This parameterization is sufficient given the current signal-to-noise ratio.

The mean density inside projected radius  $R$  then can be obtained via

$$\Sigma(\leq R) = \frac{2}{R^2} \int_0^R y dy \Sigma(y|R_{sig}), \quad (19)$$

and the final ESD is again

$$\Delta\Sigma(R) = \Sigma(\leq R) - \Sigma(R). \quad (20)$$

For the two halo term, we first generate the powerspectrum at the mean redshift of each sample using pyCamb (Lewis 2013), and then convert it to correlation function as in Luo et al. (2018). The bias model is taken from Tinker et al. (2010).

$$\xi_{hm} = \langle b_h \rangle \eta \xi_{mm}, \quad (21)$$

where

$$\eta(r) = \frac{(1 + 1.17\xi_{mm}(r))^{1.49}}{(1 + 0.69\xi_{mm}(r))^{2.09}}. \quad (22)$$

And the halo bias term  $\langle b_h \rangle$  is the effective bias (Mandelbaum et al. 2005) so that

$$\begin{aligned} \langle b_h \rangle &= (1.0 - f_{\text{sat}}) b_h(M_{\text{cen}}) \\ &+ f_{\text{sat}} \int_0^\infty n(M_h) \langle N_{\text{sat}} \rangle (M_h) b_h(M_h) dM_h. \end{aligned} \quad (23)$$

The ESD from two halo term is then calculated from the matter-matter correlation given a bias term

$$\Sigma(R) = 2\bar{\rho} \int_R^\infty [1 + \langle b_h \rangle \xi_{mm}(r)] \frac{r dr}{\sqrt{r^2 - R^2}}, \quad (24)$$

and

$$\Sigma(\leq R) = \frac{4\bar{\rho}}{R^2} \int_0^R y dy \int_y^\infty [1 + \langle b_h \rangle \xi_{mm}(r)] \frac{r dr}{\sqrt{r^2 - y^2}}, \quad (25)$$

so the two halo term is

$$\Delta\Sigma(R)_{2\text{halo}} = \Sigma(\leq R) - \Sigma(R). \quad (26)$$

Finally, we build the likelihood function and run the MCMC (Monte Carlo Markov Chain) to estimate the posterior using *emcee*<sup>4</sup>, which implements the affine

variant sampler of Goodman & Weare (2010). We assume a Gaussian likelihood with

$$\ln\mathcal{L} = -0.5[\mathbf{X}^T \mathbf{C}^{-1} \mathbf{X}], \quad (27)$$

where  $\mathbf{X} = \mathbf{D} - \mathbf{Model}$  is the difference between data vector and model,  $\mathbf{X}^T$  denotes the transpose of  $\mathbf{X}$ , and  $\mathbf{C}^{-1}$  is the inverse of covariance matrix.

## 5. RESULTS

We present the galaxy-galaxy lensing measurements of AGNs, the posterior probability distribution of the parameters in our model fit, and the stellar mass-halo mass relation of AGNs relative to the inactive galaxy population.

### 5.1. Weak lensing signal

In Figure 3, we show the galaxy-galaxy lensing signal measurement for the full AGN sample using the HSC-SSP S16A shape catalog. Given the AGN sample size, we are able to measure the lensing signal in ten spatial bins. We find a highly significant lensing signal that drops off smoothly out to 2 Mpc h<sup>-1</sup>.

For comparison, the ESD of a large inactive sample of galaxies is displayed in color, split into six different stellar mass bins. The ESDs are weighted according to the map of the stellar mass-redshift 2D distribution. As expected, the strength of the ESD signals for galaxies increases as a function of stellar mass. At smaller scales, the ESD of the AGN sample lies between the lensing profile of two most massive galaxy bins ( $\log(M_*/M_\odot) = 10.61 - 10.97$ ). However, it drops down towards the profile of the less massive galaxies at larger scales (two last bins;  $> 300$  kpc/h). This is mainly caused by differences in the satellite fractions. For lower stellar mass halos of the galaxy control sample, the satellite fraction increases thus causing a flattening of the ESD at larger scales. Such behavior is not evident in the AGN sample (Fig. 3). These effects at these scales ( $\sim 0.3$  to 1 Mpc h<sup>-1</sup>) are not likely caused by the two halo term. We elaborate further on this in Section 5.3.

We then plot in Figure 4 the ESD of the AGN sample split into two bins of stellar mass of their host galaxies ( $\log(M_*/(M_\odot)) < 10.65$  and  $\log(M_*/(M_\odot)) > 10.65$ ) to ensure similar number of lenses, hence the SNR of the lensing signals. The galaxy control sample is shown for comparison using the same mass bins, which result in having the same mean redshift and stellar mass to their AGN counterpart after weighting. We find that the ESD of high mass galaxies (control sample) is significantly higher than AGNs with the same stellar mass hosts. This means that the halo mass of the control sample

<sup>4</sup> <https://emcee.readthedocs.io/en/stable/>



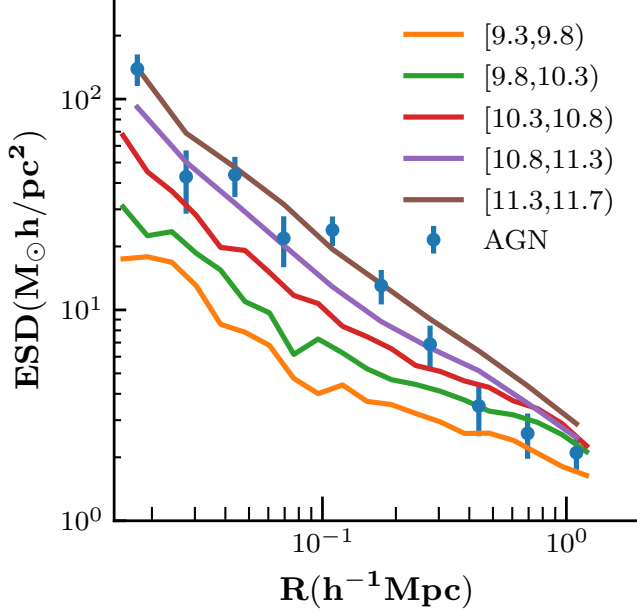


**Figure 3.** Lensing mass profile (ESD) for the full AGN sample (black circles) and the **weighted** control galaxy sample binned in stellar mass. The digits in the legend are the stellar mass range in  $\log(M_*/h^{-2}M_\odot)$ .

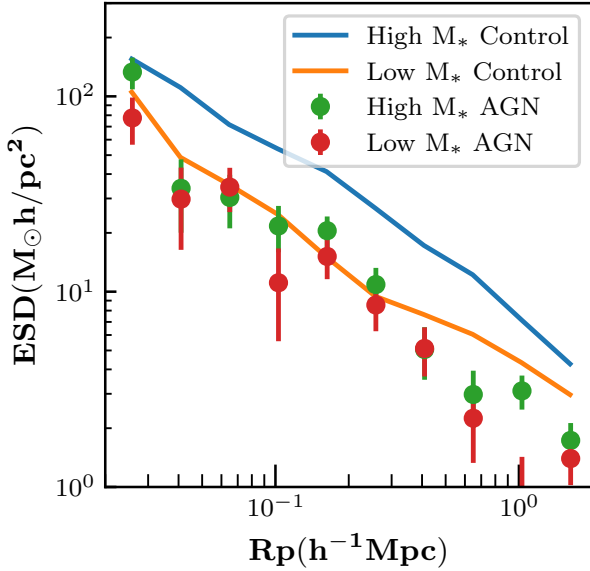


**Figure 4.** Lensing mass profile (ESD) of AGNs split by the stellar mass of their host galaxy as indicated.

is much larger than the AGN counterpart of the same stellar mass. However, the AGN and control galaxies, matched at lower stellar mass, are nearly equivalent thus sharing the same environments.

### 5.2. Lensing signal for AGN subsamples

We further divide the AGN sample by their properties including AGN luminosity, type (obscured vs. unobscured), and redshift. The left panel of Fig. 5 compares the ESDs of AGN type I (unobscured; solid dots) and type II (obscured; empty circles). The ESDs of type II AGNs are similar to the type I at most scales with the exception of the medium scales roughly from 70 kpc/h to 300kpc/h. This results in a slightly larger halo mass estimation for type II AGNs. This may be due to a selection effect such as the inclusion of only the more luminous type II AGNs. There is still some uncertainty in the difference between the two classes of AGN given the considerable errors. However, we do not rule out the possibility that there is a real difference that needs to be further investigated. We reserve such analysis for a future study since this is not the main focus of this work.

For the other two parameters (AGN luminosity and redshift), we find no statistical difference between the subsamples. We note that the uncertainty in the photometric redshifts may wash out any weak redshift and luminosity dependence of the mass profiles. These dependencies can be further explored with the larger survey area ( $\sim 4\times$ ) of the HSC shape catalog in S19A (Li et al. 2021b). Even so, we report on their difference in terms of halo mass in the Discussion.

### 5.3. Halo mass profile modelling

Using the model ESDs as described in Section 4, we decompose the contribution of the ESDs into different components: the central galaxy as an NFW profile, satellite galaxies, stellar mass of the host galaxy, and the two-halo term. We fix the stellar mass as described in Sec. 4, Eq. 11 and Eq. 26. In Fig. 6 and the upper left panel of Figure 7, we show the different contributions to the model fit for AGNs and control sample respectively. The black solid line is the total signal combining all contributions. As shown, the stellar component (red solid line) only contributes at small scales ( $< 500$  kpc  $h^{-1}$ ). The host halo is the dominant term (solid blue curve). The satellite contribution (solid green curve) is shown at relatively large scales within the virial radius. As mentioned earlier, a larger satellite fraction leads to an upturn at larger scales and flattens the overall profile.

First, we demonstrate the accuracy of the model fits to the ESD of the control galaxy sample in Figure 7 using six bins of stellar mass. The best-fit parameters are listed in Table. 2 with one-sigma errors from the posterior distribution of the MCMC process. Fig. 8 shows an example of the corner plot of the three parameters of low AGN luminosity sample with largest  $f_{\text{sat}}$  value.

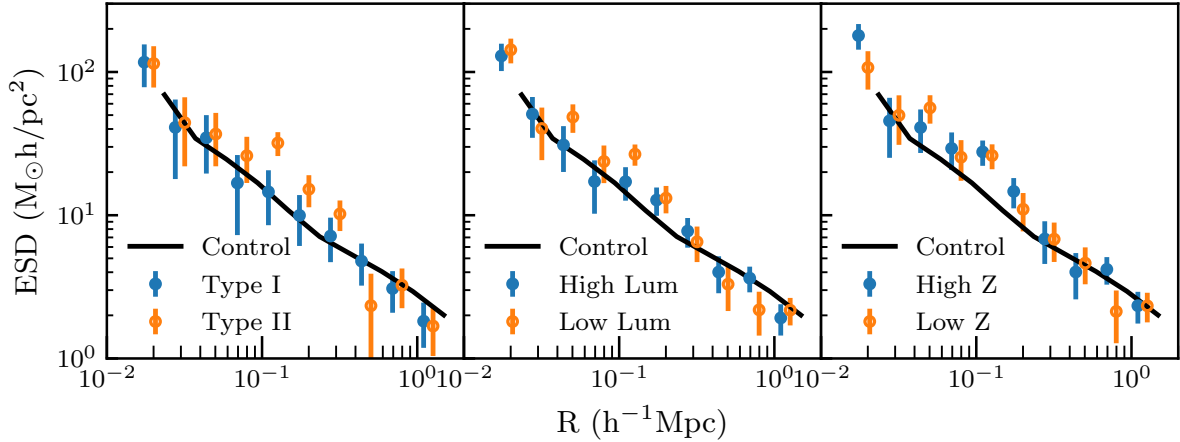


**Figure 5.** Galaxy-galaxy lensing signal (ESD) of AGN split by type (left), luminosity (middle) and redshift (right). The black solid lines are the results from control sample as reference.

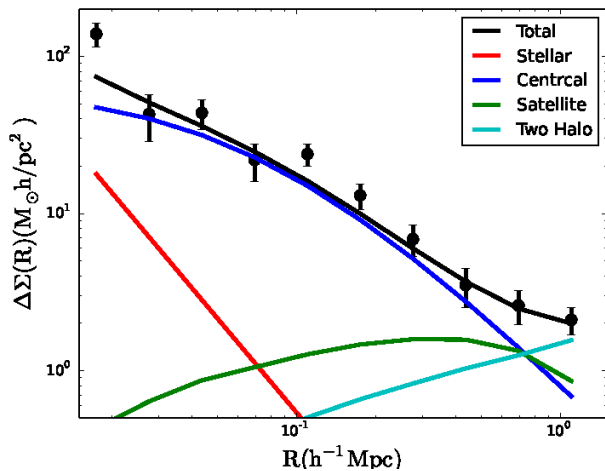


**Figure 6.** Modelling the lensing mass profile (ESD) of AGN as a whole. We plot the different contributions to the ESDs using different colors, i.e., stellar mass (red solid line), Central galaxy as NFW (blue), satellite contribution (green) and two halo term (cyan).

Based on our modeling procedure (Section 4), the AGNs typically reside in halos with a characteristic mass of  $\log(M_h/h^{-1}M_\odot) = 12.22$  (Table 2). This halo mass is close to other published studies where our value is about 0.3dex lower than X-ray detected AGN (Leauthaud et al. 2015), and 0.3 dex higher than the SDSS optically-selected AGNs (Mandelbaum et al. 2005; Zhang et al. 2020).

#### 5.4. Stellar-to-halo mass relation (SHMR) of AGNs

With the halo mass estimated from both the AGN and galaxy (control) samples, we measure the stellar-to-halo mass relation and compare with relations from published observations. In Fig. 9, the two solid lines are

from Leauthaud et al. (2010). The blue and orange color represents high (0.74-1.0) and low (0.48-0.74) redshift bins. The results for the control galaxy samples are shown as the black data points.

Overall, the SHMR of our galaxy control sample follows the trend of both calibrated relations. However, this is not exactly the case for the halo mass of our AGN sample. While the halo mass of the AGNs having lower stellar mass of their hosts (green data points) agrees with the well-established relations, the halo mass of the AGNs with high stellar mass for their hosts (red data points) is  $3.3\sigma$  lower in  $\log(M_h/h^{-1}M_\odot)$ . Both of them favor a halo mass  $M_h \sim 1.12 - 1.74 \times 10^{12} h^{-1} M_\odot$ . The halo mass of AGN as a whole are located above and below the knee of SHMR, which is considered to be the most efficient sweet spot for star formation and gas accretion (Mo et al. 2010).

## 6. DISCUSSION

The AGN-halo connection has been extensively studied in literature. For example, Li et al. (2006) claim that the halos of narrow-line AGN have a mass range from  $10^{12} - 10^{13} h^{-1} M_\odot$ , roughly spanning the peak in the stellar-to-halo mass relation, based on the projected cross-correlation between AGNs and a reference galaxy sample from SDSS DR4. By combining clustering and galaxy-galaxy lensing, Mandelbaum et al. (2009) reported that the radio-loud AGNs reside in halo masses at  $1.6 \times 10^{13} h^{-1} M_\odot$ , which is twice as massive than their radio-quiet counterparts at  $8 \times 10^{12} h^{-1} M_\odot$ . Building on this, Zhang et al. (2021) used SDSS DR7 shape catalog (Luo et al. 2017) to improve the halo estimation by modeling both galaxy-galaxy lensing signal and the ratio among projected cross-correlation samples containing mostly central type II AGNs due to selection

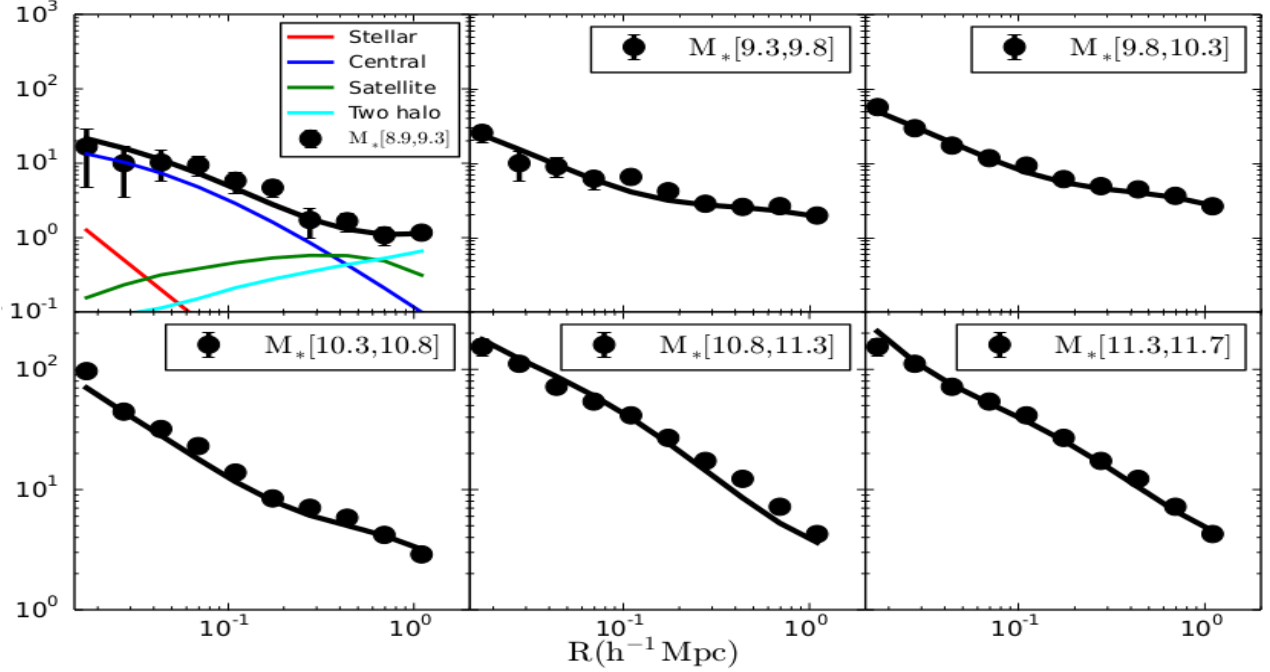


**Figure 7.** Modelling the lensing mass profile (ESD) of control galaxies split by the stellar mass. We plot the different contributions to the ESDs in the upper left panel using different colors, i.e., stellar mass (red solid line), Central galaxy as NFW (blue).  $M_*$  here denotes  $\log(M_{\text{star}}/h^{-2}M_{\odot})$

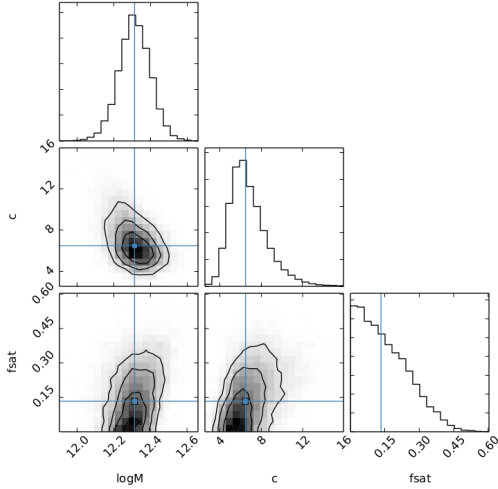


**Figure 8.** The corner plot of the three parameters of the AGN low luminosity sample. The constraints on the satellite fraction is not as strong as other two parameters.

method; the halo mass of full (irrespective of their radio loudness) AGN sample is  $\log(M_h/h^{-1}M_{\odot}) = 11.98^{+0.06}_{-0.07}$ .

Using an X-ray selected sample, [Leauthaud et al. \(2015\)](#) extract the halo mass from the galaxy-galaxy lensing technique of 382 moderate luminosity AGN at  $z < 1$ , including both obscured and unobscured cases, from the 2 square degree COSMOS field. The halo mass is  $\log(M_h/h^{-1}M_{\odot}) = 12.5$ , comparable to optically-

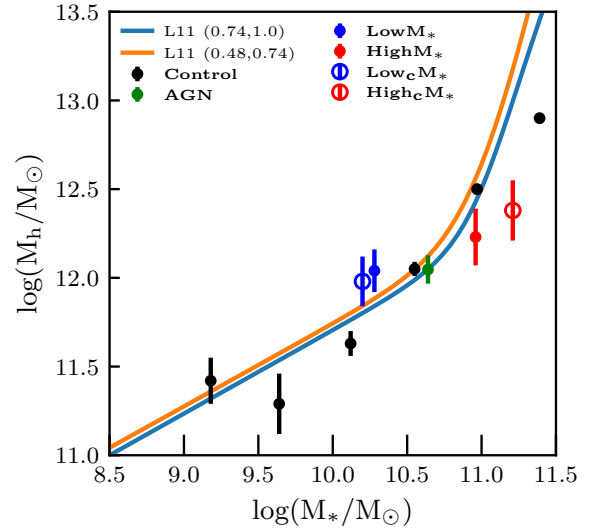


**Figure 9.** SMHR of the AGN and control galaxy samples. The theoretical lines are from Leauthaud et al. (orange and blue solid lines). The black data points show the control galaxy sample in six mass bins. The green **circle** is the result based on the full AGN sample. The low/high stellar mass AGN results are denoted as blue/red circles. The empty blue/red circles are the low/high stellar mass AGN samples with larger separation in stellar mass.

selected AGN samples. Likely more relevant to our HSC study, [Hickox et al. \(2011\)](#) presented the clustering

property of mid-infrared-selected AGN, using a sample in the redshift range  $0.7 < z < 1.8$  selected from the 9 square degree Boötes multiwavelength survey. They found that the halo mass of type II (obscured) QSOs is larger than that of type I (unobscured) QSOs with  $\log(M_h/h^{-1}M_\odot) = 13.3, 12.7$  respectively which may pose a challenge to unified models of AGN viewing angles or represent an earlier obscured growth phase with a longer duty cycle than the unobscured state.

Our effort based on galaxy-galaxy lensing using HSC finds that the characteristic halo mass of optical + mid-IR selected (HSC and WISE) AGNs is  $\log(M_h/h^{-1}M_\odot) = 12.22^{+0.08}_{-0.10}$ , right at the knee of SHMR. There is marginal difference in the typical halo mass with AGN luminosity (Fig. 5 *middle* panel) where the high luminosity cases have slightly lower halo mass than that of low-luminosity AGN samples. For a proper comparison, we re-weight the control galaxy samples using the  $M_*$  – redshift distribution of the high/low AGN luminosity samples; the halo mass of these two control samples have similar halo mass within their one sigma error, which are  $\log(M_h/h^{-1}M_\odot) = 12.19^{+0.07}_{-0.03}$  and  $\log(M_h/h^{-1}M_\odot) = 12.17^{+0.03}_{-0.03}$  while the difference is 0.44 dex for the AGN sample which is 1.2 sigma difference.

The mean stellar masses of type I AGNs are larger than that of type II AGNs, which disagrees with the results from Zou et al. (2019). This may be due to the different classification methods, the latter uses the  $\text{FWHM} > 2000$  km/s of at least one emission line criterion to define type I AGN and the rest are type II for X ray detected points sources cross-identified in Chandra Cosmos Legacy Survey. Goulding et al. (2018) uses the UV/optical color cut assuming that the characteristic tail of the AGN accretion disk is absent for type II. This selection also leads to the difference on stellar mass distribution. In order to take the selection effect into account in the galaxy-galaxy lensing measurement, we re-weight the  $M_*$  – redshift distribution of the type I AGNs to match that of type II AGNs as we have done for the control galaxy sample. Prior to this re-weighting scheme, the halo mass of type I AGN sample is the same with that of type II AGN sample within  $1\sigma$ . After re-weighting, the halo mass of type I decreases to  $\log(M_h/h^{-1}M_\odot) = 11.4^{+0.32}_{-0.27}$ . We will further explore this issue with HSC-SSP Y3 shape catalog (Li et al. 2021c)

Finally, similar to clustering results, we do not observe any redshift dependence of the halo mass of our AGN sample. The lensing profile in two different redshift bins are indistinguishable within one sigma error (Figure 10 right panel). This is in agreement with Aird &

Coil (2021b), who applies semi-analytical approach to populate AGNs in the UNIVERSEMACHINE catalog Behroozi et al. (2019). They found that the halo mass of AGNs have no redshift dependence for AGNs with  $L_X > 10^{42}$  ergs/s whereas the halo mass of controlled galaxies increase about 0.3dex from redshift above 2 to 0.2. They also found no  $L_X$  dependence on the halo mass at redshift 0.75. The halo mass of high/low AGN luminosity sample are not distinguishable within  $1\sigma$  level after reweighting the high luminosity sample. We will further explore such issues based on future HSC-SSP shape catalog (Li et al. 2021c) to pin down this difference.

A picture may be emerging where SMBHs accretion prefer to reside in environment with plentiful gas supplies. This can be understood based on our comparison of luminous AGNs with a mass-matched control sample. For the higher stellar mass bins, the characteristic halo mass is significantly lower than the SHMR. And the satellite fraction  $f_{sat}$  for the AGN samples in our study are also lower than the control samples which is opposite to the conclusion in Zhang et al. (2021). However, the constraint of the satellite fraction is not strong as shown in Fig. 10. The satellite fraction of AGN sample as whole is about  $3^{+4}_{-2}\%$ . Compared to the control sample, the satellite fraction of AGN is low, that caused the smaller signal at larger scale as we described in Sec. 5. Besides, this fraction is three times lower than that of Allevato et al. (2019), who claims that their AGNs selected from Chandra Cosmos Legacy Survey can reach up to 15% with halo mass around  $\log(M_h/h^{-1}M_\odot) \approx 13.0$ . We can think of this as follows. For any galaxy of such high stellar mass to have any gas left for accretion onto a SMBH, it is more likely to have retained that fuel if residing in a lower density environment. This is consistent with environmental studies of X-ray AGN up to  $z \sim 1$  in COSMOS (Silverman et al. 2009b) and optically-selected AGNs in SDSS (Kauffmann et al. 2004).

### 6.1. Consideration of uncertainties on the stellar mass measurements for AGN host galaxies

To address the issue of uncertainties on stellar mass measurements of AGN host galaxies, we compare the values used here, based on SED fitting (Goulding et al. 2018), with those obtained independently through 2D decomposition of HSC images (Li et al. 2021a). The latter are based on a sample of type-1 quasars that do not represent the more obscured population which are included in this study. However, they have been tested to be robust through extensive simulations and represent the most likely problematic cases where a luminous

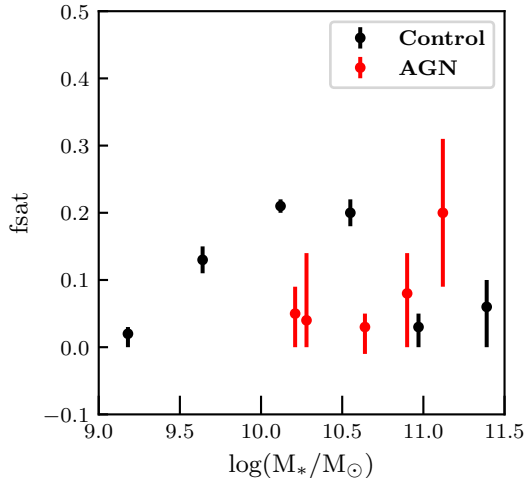


**Figure 10.** The satellite fraction of controlled galaxy sample (black dots) and the AGNs (red dots) as a function of stellar mass. The AGN samples contain low/high stellar mass sample, the AGN sample as a whole as well as the low/high stellar mass sample with larger separation as in Fig. 9.

quasar may impact the SED approach. Even though, Li et al. (2021a) claim a 0.3 dex scatter as calibrated using simulations. Thus, we may find considerable scatter by comparing the two stellar mass estimations.

In Figure 11, we show the comparison which demonstrates that this subsample follows the one-to-one relation thus there is no sign of a severe systematic offset. However, there is considerable scatter, 0.48 dex above  $10^{10} M_{\odot}$  which can impact our results if there is no further scatter between stellar mass and halo mass relation. The latter will not impact the halo mass estimation as we will address in the next paragraph. To gauge the impact of such dispersion on our results, we define a higher-mass sample with  $11.0 < M_{*} < 12.0$  which is high enough to overcome uncertainties in the mean mass by a factor of 2.5 as compared to the lower mass bin ( $9.5 < M_{*} < 10.5$ ) if the masses from the Li et al. catalog are more accurate. We re-run the analysis for this high-mass sample and confirm that there is no impact on our results as shown in the bottom panel in Fig. 11.

We carry out a Monte Carlo simulation to test the effect of the scatter of stellar mass on halo mass estimation. The Monte Carlo simulations simply takes the stellar mass function from Ilbert et al. (2013) the stellar mass halo mass relation from Leauthaud et al. (2012) to assign each Monte Carlo random sampled ‘galaxy’ with a halo mass. We specifically select two massive stellar mass bins ( $\log M_{*} \in [10.4, 10.80]$  and  $[10.80, 11.2]$  with the mean stellar mass of 10.61 and 10.97) and assign 0.35dex Gaussian random error to the two stellar mass

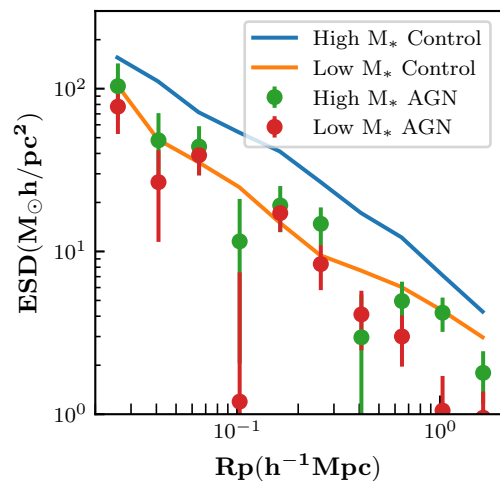
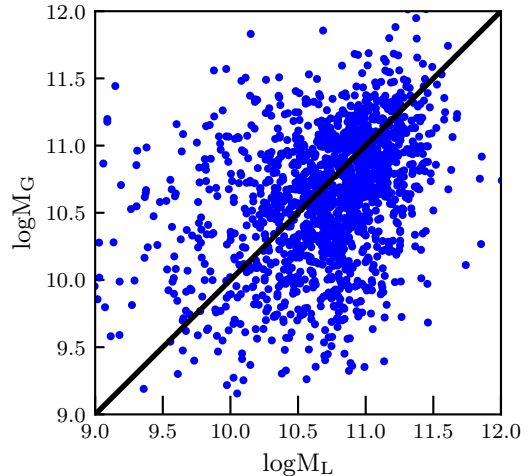


**Figure 11.** *Upper:* Comparison of independent estimates of the stellar mass of the AGN host galaxies (x-axis: Li et al. (2021a); y-axis: Goulding et al. (2018)). The black solid line is the on-to-one relation. The red vertical lines are the 10.65 threshold we used to split the AGN sample. *Lower:* The ESDs of the low(red)/high(green) stellar mass samples with larger stellar mass difference.

bins mock catalogs and calculate the mean stellar mass and mean halo mass of each bin. We found that the 0.35 dex scatter only causes 0.04 dex suppression of the mean halo mass. So our results are robust with different stellar mass estimations. This agrees with a recent study Yang et al. (2021), who shows the scatter on total luminosity of galaxy groups has little impact on the halo mass estimation.

The halo mass of whole AGNs sample locates at the stellar mass to halo mass relation curve. After we separate the sample into high/low stellar mass bins, the halo mass of the high stellar mass bin deviates from the relation and even lower than that of the control sample as shown in the upper panel of Fig. 9.

In future, as more data available from HSC-SSP. The SNR of high redshift AGN samples can be improved by a factor of four due to larger survey regions. We will continue this study with larger data sample which enables finer stellar mass bins.

## 7. SUMMARY AND CONCLUSIONS

We use an AGN sample from matched HSC and WISE catalogs (Goulding et al. 2018) to measure the summed galaxy-galaxy lensing signal in terms of Excess Surface Density (ESD). The ESDs of the AGNs are measured based on HSC-SSP S16A shape catalog. The sample size of AGNs allows us to subdivide the sample into type I/II, high/low stellar mass, high/low redshift and high/low AGN luminosity. For comparison, we build a control sample of galaxies from HSC-SSP S16A fields matching the stellar mass and redshift distributions of the AGN sample based on a weighting scheme. The ESD of the control galaxies is measured in six bins of stellar mass. The ESDs are summarised as follows:

1. We measure the galaxy-galaxy lensing signals, ESDs around AGN samples and controlled galaxy samples. We found that the ESDs of AGNs show steeper decrease at larger scale which is due to the smaller satellite fraction. This results differs from Zhang et al. (2021) who found stronger clustering for AGNs than starforming galaxies at smaller scale.
2. We split the AGNs by stellar mass and found the halo mass does not change as the halo mass in control galaxy sample. In order to further minimize the scatter in AGN stellar mass estimation, we split the AGN sample using a conservative measures so that the mean stellar mass of the two samples differs from each other at one magnitude level. The ESDs does not show any significant change.
3. We also try different sample selection based on luminosity, type and redshift. We did not find any significant difference from these subsamples.

We further build a model to extract the information of halo mass, concentration, satellite HOD, and satellite fraction. We run MCMC using emcee to sample the posterior distributions of each parameter. We find that the halo mass is very sensitive to the ESDs as expected while the concentration parameter and amplitude in the simple power-law satellite HOD are not. The satellite fraction is relatively well constrained in the control sample thanks to the high SNR ESDs measurements. We summarize our main results as follows:

1. The mean halo mass of the full AGN sample is  $\log(M_h/h^{-1}M_\odot)=12.22^{+0.08}_{-0.10}$ . The AGN are located at the knee of the stellar mass and halo mass relation, where star formation is the most efficient.
2. The mean halo mass of the galaxy control sample follows the trend of the calibrated SHMR as in Fig. 9. This shows our model reasonably extracts the halo mass information. One interesting discovery in our work is that the halo mass of high stellar mass AGN sample  $\log(M_h/h^{-1}M_\odot) = 12.24^{+0.15}_{-0.22}$  is about  $1.5\sigma$  lower than the calibrated SHMR. Meanwhile the halo mass  $\log(M_h/h^{-1}M_\odot) = 12.05^{+0.12}_{-0.14}$  of the low stellar mass AGN is comparable to the established SHMR.
3. The type I and type II AGNs have marginally distinguishable halo mass given the same stellar mass and redshift distribution. The halo mass of type I AGN is  $1.98\sigma$  lower from type II. The halo mass of high AGN luminosity sample also shows a lower halo mass than the low AGN luminosity sample, but due to the low SNR the two halo masses are still within one sigma error. We also re-weight the galaxy control sample to the  $M_* - z$  distribution of type II AGN and the low luminosity AGN sample. We do not find significant difference between type II AGNs, low-luminosity AGNs, and the galaxy control sample.
4. The satellite fraction of the control sample is generally larger than our AGN sample. The AGN sample as a whole has a  $3^{+4}_{-2}\%$  of satellite fraction, which explains the lower ESD signal than the control galaxy sample at larger scale.

In future, we expect to measure the higher SNR galaxy-galaxy lensing signals from HSC-SSP Y3 shape catalog. With the higher SNR signals, we are able to explore more the halo properties of AGNs with finer binning scheme. Besides the IR-optical selected AGNs, we can also compare the X-ray selected AGNs with that of the sample we used in this work.

We thank the anonymous referee for her/his valuable feedback that significantly improve the contents of our work. We also thank Zheng Zheng from the University of Utah for valuable discussions of HOD modeling. WL acknowledge the support from the National Key R&D Program of China (2021YFC2203100), NSFC(NO. 11833005, 12192224) and World Premier International Research Center Initiative (WPI Initiative), MEXT, Japan. JS is supported by JSPS KAKENHI Grant Number JP18H01251 and the World Premier International Research Center Initiative (WPI), MEXT, Japan. All numerics are operated on the computer gfarm cluster at Kavli IPMU, the University of Tokyo.

## REFERENCES

- Ahumada, R., Allende Prieto, C., Almeida, A., et al. 2020, *ApJS*, 249, 3
- Aihara, H., Armstrong, R., Bickerton, S., et al. 2018, *PASJ*, 70, S8
- Aihara, H., AlSayyad, Y., Ando, M., et al. 2019, *PASJ*, 71, 114
- Aird, J., & Coil, A. L. 2021a, *MNRAS*, arXiv:2010.02957
- . 2021b, *MNRAS*, arXiv:2010.02957
- Alam, S., Ross, N. P., Eftekharzadeh, S., et al. 2020, arXiv e-prints, arXiv:2007.02612
- Allevato, V., Viitanen, A., Finoguenov, A., et al. 2019, *A&A*, 632, A88
- Becker, R. H., White, R. L., & Helfand, D. J. 1995, *ApJ*, 450, 559
- Behroozi, P., Wechsler, R. H., Hearin, A. P., & Conroy, C. 2019, *MNRAS*, 488, 3143
- Behroozi, P. S., Wechsler, R. H., & Wu, H.-Y. 2012, *The Astrophysical Journal*, 762, 109
- Bertin, E. 2011, in *Astronomical Society of the Pacific Conference Series*, Vol. 442, *Astronomical Data Analysis Software and Systems XX*, ed. I. N. Evans, A. Accomazzi, D. J. Mink, & A. H. Rots, 435
- Bosch, J., Armstrong, R., Bickerton, S., et al. 2018, *PASJ*, 70, S5
- Bruzual, G., & Charlot, S. 2003, *MNRAS*, 344, 1000
- Calzetti, D., Armus, L., Bohlin, R. C., et al. 2000, *ApJ*, 533, 682
- Cappelluti, N., Brusa, M., Hasinger, G., et al. 2009, *A&A*, 497, 635
- Carraro, R., Rodighiero, G., Cassata, P., et al. 2020, *A&A*, 642, A65
- Carrasco Kind, M., & Brunner, R. J. 2014, *MNRAS*, 438, 3409
- Chabrier, G. 2003, *ApJL*, 586, L133
- Condon, J. J., Cotton, W. D., Greisen, E. W., et al. 1998, *AJ*, 115, 1693
- Cunha, C. E., Lima, M., Oyaizu, H., Frieman, J., & Lin, H. 2009, *MNRAS*, 396, 2379
- DiPompeo, M. A., Hickox, R. C., Eftekharzadeh, S., & Myers, A. D. 2017a, *MNRAS*, 469, 4630
- . 2017b, *MNRAS*, 469, 4630
- Eftekharzadeh, S., Myers, A. D., White, M., et al. 2015, *MNRAS*, 453, 2779
- Elvis, M., Civano, F., Vignali, C., et al. 2009, *ApJS*, 184, 158
- Folkes, S., Ronen, S., Price, I., et al. 1999, *MNRAS*, 308, 459
- Goodman, J., & Weare, J. 2010, *Communications in Applied Mathematics and Computational Science*, 5, 65
- Górski, K. M., Hivon, E., Banday, A. J., et al. 2005, *ApJ*, 622, 759
- Goulding, A. D., Greene, J. E., Bezanson, R., et al. 2018, *PASJ*, 70, S37
- Hasinger, G., Altieri, B., Arnaud, M., et al. 2001, *A&A*, 365, L45
- Hickox, R. C., Myers, A. D., Brodwin, M., et al. 2011, *ApJ*, 731, 117
- Hirata, C., & Seljak, U. 2003, *MNRAS*, 343, 459
- Hopkins, P. F., Cox, T. J., Kereš, D., & Hernquist, L. 2008, *ApJS*, 175, 390
- Hsieh, B. C., & Yee, H. K. C. 2014, *ApJ*, 792, 102

**Table 2.** Posterior of parameters we fitted to ESD signals with five parameters.

Sample	$\log(M_h/h^{-1}M_\odot)$	Concentration(c)	$f_{sat}$
AGN all	$12.22^{+0.08}_{-0.10}$	$6.6^{+2.1}_{-1.5}$	$0.03^{+0.04}_{-0.02}$
AGN I	$11.85^{+0.28}_{-0.37}$	$6.3^{+6.7}_{-3.3}$	$0.12^{+0.07}_{-0.07}$
AGN I(wt)	$11.41^{+0.32}_{-0.37}$	$6.9^{+6.9}_{-5.8}$	$0.12^{+0.07}_{-0.07}$
AGN II	$12.28^{+0.10}_{-0.12}$	$7.1^{+2.7}_{-1.9}$	$0.04^{+0.05}_{-0.03}$
AGN lowz	$12.20^{+0.11}_{-0.13}$	$9.3^{+3.7}_{-2.5}$	$0.07^{+0.07}_{-0.05}$
AGN highz	$12.04^{+0.16}_{-0.22}$	$7.7^{+5.7}_{-3.0}$	$0.06^{+0.05}_{-0.04}$
AGN lowMs	$12.05^{+0.12}_{-0.14}$	$10.4^{+4.7}_{-3.2}$	$0.04^{+0.04}_{-0.10}$
AGN highMs	$12.24^{+0.15}_{-0.22}$	$4.6^{+2.7}_{-1.5}$	$0.08^{+0.08}_{-0.06}$
AGN lowL	$12.31^{+0.09}_{-0.08}$	$6.6^{+2.0}_{-1.5}$	$0.14^{+0.13}_{-0.10}$
AGN highL	$11.87^{+0.28}_{-0.35}$	$7.6^{+2.0}_{-1.5}$	$0.12^{+0.07}_{-0.07}$
AGN highL(wt)	$12.02^{+0.34}_{-0.49}$	$10.7^{+6.1}_{-5.7}$	$0.12^{+0.07}_{-0.07}$
GMSbin 1	$11.43^{+0.12}_{-0.16}$	$6.1^{+3.4}_{-2.0}$	$0.02^{+0.02}_{-0.01}$
GMSbin 2	$11.29^{+0.18}_{-0.17}$	$6.0^{+4.6}_{-2.5}$	$0.13^{+0.02}_{-0.02}$
GMSbin 3	$11.63^{+0.07}_{-0.06}$	$10.1^{+2.9}_{-2.2}$	$0.21^{+0.01}_{-0.01}$
GMSbin 4	$12.06^{+0.04}_{-0.04}$	$10.7^{+1.4}_{-1.2}$	$0.20^{+0.02}_{-0.02}$
GMSbin 5	$12.50^{+0.03}_{-0.03}$	$7.6^{+0.9}_{-0.8}$	$0.03^{+0.03}_{-0.02}$
GMSbin 6	$12.90^{+0.03}_{-0.03}$	$4.9^{+0.6}_{-0.5}$	$0.06^{+0.06}_{-0.04}$
GLowAGN	$12.16^{+0.03}_{-0.03}$	$6.92^{+0.5}_{-0.5}$	$0.10^{+0.004}_{-0.004}$
GTypeII	$12.22^{+0.03}_{-0.03}$	$4.58^{+0.4}_{-0.4}$	$0.11^{+0.016}_{-0.018}$

Ilbert, O., McCracken, H. J., Le Fèvre, O., et al. 2013, A&A, 556, A55

Inoue, A. K. 2011, MNRAS, 415, 2920

Ishibashi, W., Fabian, A. C., & Arakawa, N. 2021, MNRAS, 502, 3638

Jiang, N., Wang, H., Mo, H., et al. 2016, ApJ, 832, 111

Juric, M., & Tyson, T. 2015, Highlights of Astronomy, 16, 675

Kauffmann, G., White, S. D. M., Heckman, T. M., et al. 2004, MNRAS, 353, 713

Khabiboulline, E. T., Steinhardt, C. L., Silverman, J. D., et al. 2014, ApJ, 795, 62

King, A., & Pounds, K. 2015, ARA&A, 53, 115

Kormendy, J., & Ho, L. C. 2013, ARA&A, 51, 511

Koutoulidis, L., Georgantopoulos, I., Mountrichas, G., et al. 2018, MNRAS, 481, 3063

Krishnan, C., Almaini, O., Hatch, N. A., et al. 2020, MNRAS, 494, 1693

Krumpe, M., Miyaji, T., Coil, A. L., & Aceves, H. 2018, MNRAS, 474, 1773

Le Fèvre, O., Vettolani, G., Maccagni, D., et al. 2005, in Multiwavelength Mapping of Galaxy Formation and Evolution, ed. A. Renzini & R. Bender, 222

Leauthaud, A., Massey, R., Kneib, J.-P., et al. 2007, ApJS, 172, 219

Leauthaud, A., Finoguenov, A., Kneib, J.-P., et al. 2010, ApJ, 709, 97

Leauthaud, A., Tinker, J., Bundy, K., et al. 2012, ApJ, 744, 159

Leauthaud, A., J. Benson, A., Civano, F., et al. 2015, MNRAS, 446, 1874

Leauthaud, A., Saito, S., Hilbert, S., et al. 2017, MNRAS, 467, 3024

Lewis, A. 2013, PhRvD, 87, 103529

Li, C., Kauffmann, G., Wang, L., et al. 2006, MNRAS, 373, 457

Li, J., Silverman, J. D., Ding, X., et al. 2021a, arXiv e-prints, arXiv:2109.02751

Li, X., Miyatake, H., Luo, W., et al. 2021b, arXiv e-prints, arXiv:2107.00136

—. 2021c, arXiv e-prints, arXiv:2107.00136

Luo, W., Yang, X., Zhang, J., et al. 2017, ApJ, 836, 38

Luo, W., Yang, X., Lu, T., et al. 2018, ApJ, 862, 4

Mandelbaum, R., Li, C., Kauffmann, G., & White, S. D. M. 2009, MNRAS, 393, 377

Mandelbaum, R., Seljak, U., & Hirata, C. M. 2008, JCAP, 2008, 006

Mandelbaum, R., Tasitsiomi, A., Seljak, U., Kravtsov, A. V., & Wechsler, R. H. 2005, MNRAS, 362, 1451

Mandelbaum, R., Miyatake, H., Hamana, T., et al. 2018a, PASJ, 70, S25

Mandelbaum, R., Lanusse, F., Leauthaud, A., et al. 2018b, MNRAS, 481, 3170

Mateos, S., Alonso-Herrero, A., Carrera, F. J., et al. 2012, MNRAS, 426, 3271



- Medezinski, E., Oguri, M., Nishizawa, A. J., et al. 2018, PASJ, 70, 30
- Mendez, A. J., Coil, A. L., Aird, J., et al. 2016, ApJ, 821, 55
- Miyatake, H., Battaglia, N., Hilton, M., et al. 2019, ApJ, 875, 63
- Mo, H., van den Bosch, F. C., & White, S. 2010, Galaxy Formation and Evolution
- Mullaney, J. R., Pannella, M., Daddi, E., et al. 2012, MNRAS, 419, 95
- Myers, A. D., Palanque-Delabrouille, N., Prakash, A., et al. 2015, ApJS, 221, 27
- Nakajima, R., Mandelbaum, R., Seljak, U., et al. 2012, MNRAS, 420, 3240
- Pâris, I., Petitjean, P., Aubourg, É., et al. 2012, A&A, 548, A66
- Planck Collaboration, Aghanim, N., Akrami, Y., et al. 2018, arXiv e-prints, arXiv:1807.06209
- Polletta, M., Tajer, M., Maraschi, L., et al. 2007, ApJ, 663, 81
- Powell, M. C., Cappelluti, N., Urry, C. M., et al. 2018, ApJ, 858, 110
- Robotham, A., Driver, S. P., Norberg, P., et al. 2010, PASA, 27, 76
- Rodríguez-Torres, S. A., Comparat, J., Prada, F., et al. 2017, MNRAS, 468, 728
- Ross, N. P., Shen, Y., Strauss, M. A., et al. 2009, ApJ, 697, 1634
- Rowe, B. T. P., Jarvis, M., Mandelbaum, R., et al. 2015, Astronomy and Computing, 10, 121
- Schulze, A., Silverman, J. D., Daddi, E., et al. 2019, MNRAS, 488, 1180
- Scoville, N., Abraham, R. G., Aussel, H., et al. 2007, ApJS, 172, 38
- Shangguan, J., Ho, L. C., Bauer, F. E., Wang, R., & Treister, E. 2020, ApJ, 899, 112
- Sheldon, E. S., Johnston, D. E., Frieman, J. A., et al. 2004, AJ, 127, 2544
- Shen, Y., Strauss, M. A., Oguri, M., et al. 2007, AJ, 133, 2222
- Shen, Y., Strauss, M. A., Ross, N. P., et al. 2009, ApJ, 697, 1656
- Shirasaki, Y., Akiyama, M., Nagao, T., et al. 2018, PASJ, 70, S30
- Silverman, J. D., Lamareille, F., Maier, C., et al. 2009a, ApJ, 696, 396
- Silverman, J. D., Kovač, K., Knobel, C., et al. 2009b, ApJ, 695, 171
- Sohn, J., Chon, G., Böhringer, H., et al. 2018a, ApJ, 855, 100
- Sohn, J., Geller, M. J., Rines, K. J., et al. 2018b, ApJ, 856, 172
- Stern, D., Assef, R. J., Benford, D. J., et al. 2012, ApJ, 753, 30
- Tanaka, M. 2015, ApJ, 801, 20
- Tanaka, M., Coupon, J., Hsieh, B.-C., et al. 2018, PASJ, 70, S9
- Tinker, J. L., Robertson, B. E., Kravtsov, A. V., et al. 2010, ApJ, 724, 878
- Tinker, J. L., Weinberg, D. H., Zheng, Z., & Zehavi, I. 2005, ApJ, 631, 41
- Wright, E. L., Eisenhardt, P. R. M., Mainzer, A. K., et al. 2010, AJ, 140, 1868
- Xie, Y., Ho, L. C., Zhuang, M.-Y., & Shangguan, J. 2021, ApJ, 910, 124
- Yang, X., Mo, H. J., van den Bosch, F. C., et al. 2006, MNRAS, 373, 1159
- Yang, X., Xu, H., He, M., et al. 2021, ApJ, 909, 143
- York, D. G., Adelman, J., Anderson, John E., J., et al. 2000, AJ, 120, 1579
- Zhang, Z., Wang, H., Luo, W., et al. 2020, arXiv e-prints, arXiv:2012.10640
- . 2021, A&A, 650, A155
- Zheng, Z., Coil, A. L., & Zehavi, I. 2007, ApJ, 667, 760
- Zou, F., Yang, G., Brandt, W. N., & Xue, Y. 2019, ApJ, 878, 11
- Zu, Y., & Mandelbaum, R. 2015, MNRAS, 454, 1161